We are IntechOpen, the world's leading publisher of Open Access books Built by scientists, for scientists

4,800
Open access books available

122,000
International authors and editors

135M
Downloads

Our authors are among the

154
Countries delivered to

TOP 1%
most cited scientists

12.2%
Contributors from top 500 universities

WEB OF SCIENCE™

Selection of our books indexed in the Book Citation Index in Web of Science™ Core Collection (BKCI)

Interested in publishing with us?
Contact book.department@intechopen.com

Numbers displayed above are based on latest data collected.
For more information visit www.intechopen.com

21

Finite element analysis of deformation and fracture of cylindrical tubes under internal moving pressures

Majid Mirzaei
Department of Mechanical Engineering, Tarbiat Modares University
Iran

1. Introduction

This Chapter presents a review of the basic formulations, solution methods, and simulation procedures that are essential in the finite element analysis of deformation and fracture of cylindrical tubes under internal moving pressures. Such analyses are applicable to a number of theoretical and practical problems, like deformation and rupture of arteries due to blood flow, cyclic fracture of gas pipelines, vibrational behavior of pulse detonation engines, etc. However, the scope of this chapter is mostly concerned with *high-speed* moving pressures that can cause significant *fluctuating* stresses in the tube wall. Based on their relative magnitudes, these stresses can result in various types of mechanical failure such as: high cycle fatigue cracking (Mirzaei et al., 2006c), low cycle fatigue & dynamic tearing (Mirzaei, 2008a; 2009), and severe dynamic fragmentation (Price, 2006; Goto et al., 2008; Soto et al., 2010).
It should be emphasized that finite element simulations of the above mentioned processes are rather difficult and not only involve judicial implementation of advanced finite element (FE) techniques but also require a clear understanding of the nature of the underlying deformation and fracture mechanisms. Hence, this chapter starts with a brief review of the basics of deformation and fracture mechanisms that are specific to this type of problems. In continuation, the pertinent FE formulations and solution methods are reviewed and a treatise of the relevant fracture mechanics parameters is presented. The final sections of this chapter are devoted to practical examples including the FE analyses of deformation and fracture of an experimental aluminum tube and an exploded steel cylinder.

2. Structural Response of Tubes to High-speed Moving Pressures

The structural response of a cylindrical tube to internal moving pressure depends on several parameters; including the dimensions and mechanical properties of the tube as well as the magnitude and speed of the moving pressure. Classical examples include *high-speed* traveling pressure waves with specific profile caused by detonation of gaseous mixtures or traveling shock waves (see Fig.1).

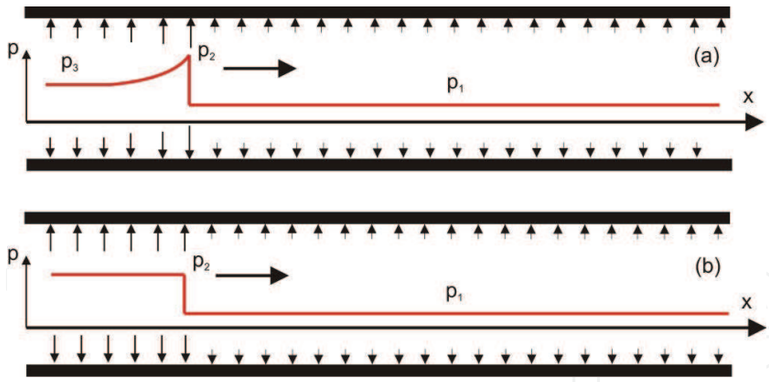

Fig. 1. Schematic of internal moving pressures a) gaseous detonation b) shock.

Grossly, we may define three pressure levels for which three different types of structural response can be expected. These pressures can be designated as low, medium, and high in relation with the magnitude of the resultant stresses which can be less than, equal to, or higher than the dynamic ultimate tensile strength of the material.

2.1 Low-Pressure Moving Front

For relatively *low pressures* (level 1) the passage of pressure front results in a pattern of fluctuating *elastic* strains which can exist even after the moving load dies out. For this case a variety of analytical, experimental, and FE solutions is available for the structural response (Tang, 1965; Reismann, 1965; Beltman et al., 1999; Beltman & Shepherd, 2002; Mirzaei et al., 2005,2006a; Mirzaei, 2008b). An interesting application for this type of moving pressure is the pulse detonation engine (PDE) which is currently regarded as a promising candidate for providing very efficient propulsion systems for both subsonic and supersonic aviation. Since the PDE generates quasi steady thrust by high cycling of gaseous detonations, the interactions between the stress waves caused by successive detonations can be troublesome and cause high-cycle fatigue cracking in the tube wall.

2.2 Medium-Pressure Moving Front

Traveling of higher pressures (level 2), that can cause stresses in the order of the ultimate tensile strength of the material, may initiate axial cracks which with further propagation can result in *limited* fragmentation of the tube wall. There was no report in the open literature about confined crack growth in tubes under gaseous detonation, prior to the experimental study reported by Chao and Shepherd (2005). Their study was primarily motivated by accidents like those occurred in the nuclear power plants in Japan (Naitoh et al., 2003) and Germany in 2001. In both incidents, sections of steel steam pipes were fragmented due to combustion of hydrogen-oxygen mixtures created by radiolysis. One of the most important questions that arose during the accident investigation was whether the type of accidental combustion can be deduced from the fracture patterns. Recently it was shown that at this pressure level a major portion of crack growth is periodic and under the influence of the fluctuating stresses. This cyclic crack growth can result in formation of special markings on the crack surfaces and has specific features (Mirzaei, 2008a). According to the schematic depicted in Fig. 2, the passage of detonation front results in a pattern of fluctuating hoop

strains which exist even after the detonation loading dies out. In presence of an axial trough-thickness crack, the points on the crack surface can continue to oscillate radially. However, because the crack surface is traction free, these points also tend to displace circumferentially under the influence of stresses imposed by the neighboring material. The outcome is that the points on the crack surface are forced to displace in the resultant direction. The continuation of this effect, which is maximum at the crack center and minimum at the crack tips, results in the bulging of crack flaps. With the extension of the bulged area, large tensile stresses (equivalent to yield stress) develop in the bulged region in the axial direction of the tube. Since cracks usually tend to grow perpendicular to the largest principal stress directions, the initial self-similar growth changes into a circumferential growth by curving around the bulged region. The occurrence of branching at this point is also possible for the cases that the energy release rate of the crack is high enough to support two crack fronts (Mirzaei, 2008a; Mirzaei et al., 2009).

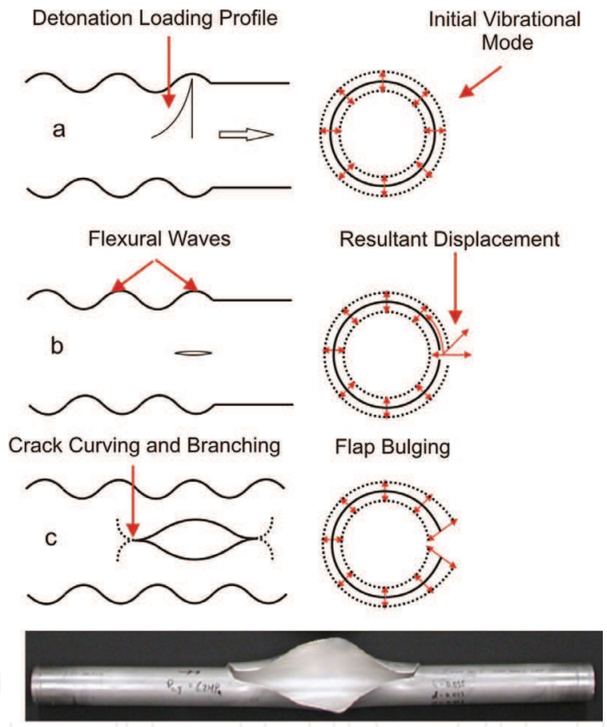

Fig. 2. Top: formation of flexural waves by a moving detonation front and the resulting flap bulging, curving, and branching (Mirzaei, 2008a). Bottom: a confined rupture of an experimental aluminum tube under internal gaseous detonation (Chao, 2004).

Unfortunately, reports on the FE simulation of detonation-driven fracture of tubes at this pressure level are not only scarce but also controversial. Due to the complexity of the process, researchers have followed two different simulation approaches. In the first approach the emphasis is essentially placed on the effects of the structural waves and the usage of dynamic fracture properties, while the probable effect of the structural behavior on the gas dynamics is ignored (Mirzaei & Karimi, 2006b; Mirzaei et al., 2009). The second approach involves coupled fluid dynamic and structural analysis using static fracture

resistance values (Cirak et al., 2007). We will discuss these issues in more detail at the end of this chapter.

2.3 High-Pressure Moving Front

For higher pressures (level 3) several cracks can initiate simultaneously and their rapid growth and branching can cause severe dynamic fragmentation. This procedure can result from both gaseous detonation (Price, 2006) and high-explosive detonation (Goto et al., 2007) (see Fig.3).

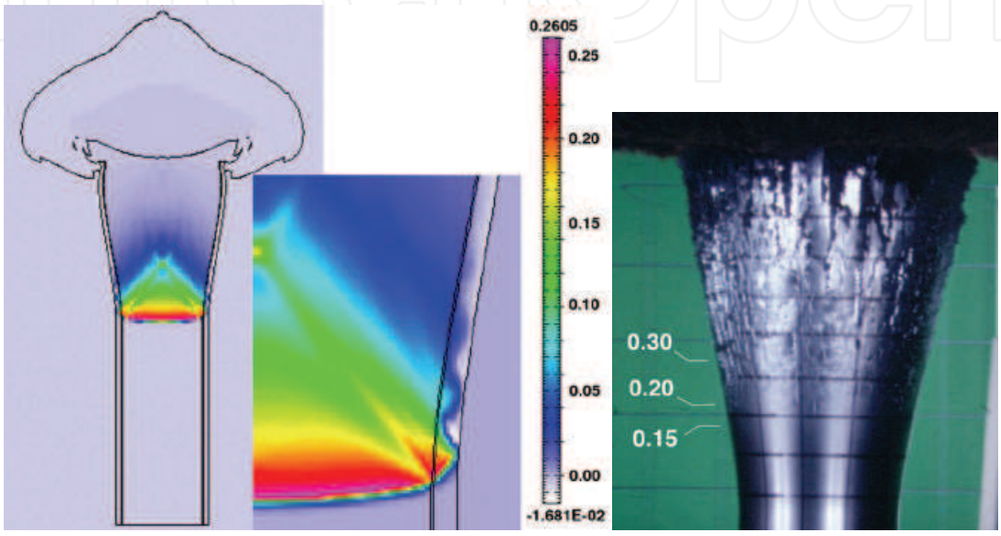

Fig. 3. Left: Computed pressure (in Mbar) in a cylinder (15 μs after detonation). Right: optical image of fragmentation 25 μs after detonation (Goto et al., 2007).

A very recent FE study of this procedure was reported by Soto et al. (2010) who proposed an efficient fluid–solid coupled finite element scheme for weapon fragmentation simulations.

3. Theoretical Aspects (an overview)

Successful simulations of deformation and fracture of cylindrical tubes not only involve a clear understanding of the underlying mechanisms but also require implementation of *transient dynamic elasto-plastic* FE formulation and specific modeling techniques. In sequel, a brief treatise of FE formulation and related fracture parameters is presented.

3.1 Finite Element Formulation

Scientists and engineers usually formulate mathematical models of physical phenomena in terms of differential equations. These ***equations*** along with the associated initial and boundary conditions form the "initial and boundary value ***problems***". In practice, finding analytical solutions for these problems is not possible for a majority of applications. The basic reason is that the solution must possess a certain degree of continuity in differentiation which is dictated by the differential equation. In other words, the differential equation places ***strong*** conditions on the solution. These strong conditions can be ***weakened*** by

recasting the differential equation in the form of certain integrals. The evaluation of these integrals can be further facilitated if the domain of the problem is subdivided into simple parts (elements). In practice, evaluation of the solution for the assemblage of these elements involves a large amount of numerical computations which can only be carried out using digital computers. The above mentioned activities constitute solution procedures which are called ***Finite Element Methods.***

3.2 A Lagrangian Nonlinear Dynamic Formulation

In this section we will review some general definitions and formulations concerning finite element equations for time-dependent and non-linear continuum problems. For analyses with large displacements, rotations, and/or strains, we need to track the position and shape of the body throughout the analysis. The Lagrangian meshes conform to and move with the material points. Thus, they are most suitable for solid mechanics problems as they can handle the complicated boundaries with relative ease. Moreover, as they have the ability to follow the material points, they are most suitable to handle the history-dependent materials. Moreover, in the Updated Lagrangian (UL) formulation, for which Eulerian measures of stress and strain are used, the derivatives and integrals are taken with respect to the spatial coordinates and the only limitation is the element capabilities to deal with large distortions. Fig. 4 shows the undeformed configuration of a material continuum at time t = t_0 together with the deformed configuration at a later time t = t.

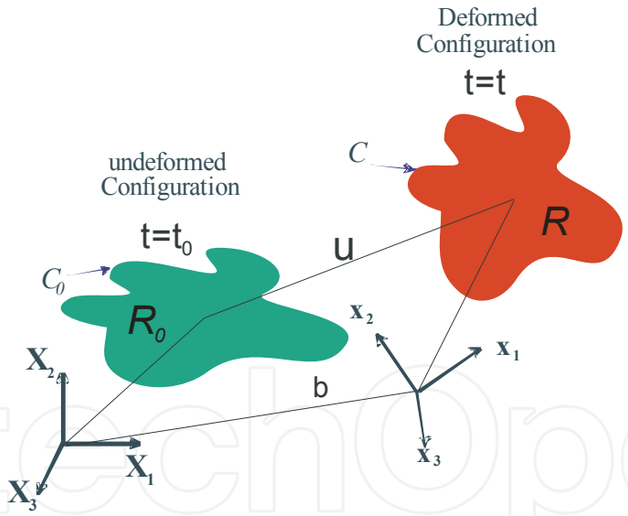

Fig. 4. Undeformed and deformed configurations of a material continuum.

We may describe the motion of the body by:

$$\mathbf{x} = \Phi(\mathbf{X}, t) \qquad or \qquad x_i = \phi_i(\mathbf{X}, t) \tag{1}$$

in which $\mathbf{x}$ denotes the spatial (Eulerian) coordinates, $\mathbf{X}$ is the material (Lagrangian) coordinates, t is time (or a time-like parameter), and Φ defines a mapping between the *initial* (undeformed) and the *current* (deformed) configurations (In the TL formulation, the initial configuration is also called the *reference* configuration since all the equations are referred to it).

Accordingly, the displacement, velocity, and acceleration can be defined as:

$$\begin{aligned}
&\mathbf{u} = \mathbf{x} - \mathbf{X} \quad or \quad \mathbf{u}(\mathbf{X},t) = \Phi(\mathbf{X},t) - \Phi(\mathbf{X},0) \\
&\mathbf{v}(\mathbf{X},t) = \frac{\partial \Phi(\mathbf{X},t)}{\partial t} = \frac{\partial \mathbf{u}(\mathbf{X},t)}{\partial t} \equiv \dot{\mathbf{u}} \\
&\mathbf{a}(\mathbf{X},t) = \frac{\partial \mathbf{v}(\mathbf{X},t)}{\partial t} = \frac{\partial^2 \mathbf{u}(\mathbf{X},t)}{\partial t^2} \equiv \dot{\mathbf{v}}
\end{aligned} \tag{2}$$

For a nonlinear dynamic problem for which we assume the *infinitesimal strain* condition the strong form is:

$$\begin{aligned}
&\sigma_{ji,j} + \rho b_i = \rho \dot{v}_i \equiv \rho \ddot{u}_i \quad in \ \Omega \\
&\text{B.C.} \begin{cases} n_i \sigma_{ji} = \overline{t}_i^*(\mathbf{x},t) & on \ \Gamma_t^* \\ u_i = \overline{u}_i^*(\mathbf{x},t) & on \ \Gamma_u^* \end{cases} \\
&\text{I.C.} \begin{cases} u_i(t=0) = u_i^0 \\ v_i(t=0) = v_i^0 \end{cases} \\
&\varepsilon_{ij} = \frac{1}{2}\left(u_{i,j} + u_{j,i}\right) \\
&\sigma_{ij} = \sigma_{ij}\left(\boldsymbol{\varepsilon}(\mathbf{u})\right)
\end{aligned} \tag{3}$$

Note that in general the stress tensor is a function of the strain tensor, which in turn is a function of displacements. The test and trial functions belong to the following spaces:

$$\begin{aligned}
&\delta v_i(\mathbf{X}) \in \mathcal{U}_0, \quad \mathcal{U}_0 = \left\{ \delta v_i \middle| \delta v_i \in C^0(\mathbf{X}),\ \delta v_i = 0 \quad \text{on} \quad \Gamma_{v_i} \right\} \\
&v_i(\mathbf{X},t) \in \mathcal{U}, \quad \mathcal{U} = \left\{ v_i \middle| v_i \in C^0(\mathbf{X}),\ v_i = \overline{v}_i \quad \text{on} \quad \Gamma_{v_i} \right\}
\end{aligned} \tag{4}$$

Taking the product of the momentum equation with a test function δv_i and integrating over the current configuration, we have,

$$\int_\Omega \delta v_i \left(\sigma_{ji,j} + \rho b_i - \rho \dot{v}_i \right) d\Omega = 0 \tag{5}$$

and the integration by parts results in:

$$\begin{aligned}
&\int_\Omega \left[\left(\delta v_i \sigma_{ji} \right)_{,j} - \delta v_{i,j} \sigma_{ji} \right] d\Omega + \int_\Omega \delta v_i \rho b_i d\Omega - \int_\Omega \delta v_i \rho \dot{v}_i \, d\Omega = 0 \\
&\int_{\Gamma_t^*} \delta v_i n_i \sigma_{ji} d\Gamma - \int_\Omega \delta v_{i,j} \sigma_{ji} d\Omega + \int_\Omega \delta v_i \rho b_i d\Omega - \int_\Omega \delta v_i \rho \dot{v}_i \, d\Omega = 0 \\
&\int_{\Gamma_t^*} \delta v_i \overline{t}_i^* d\Gamma - \int_\Omega \delta v_{i,j} \sigma_{ji} d\Omega + \int_\Omega \delta v_i \rho b_i d\Omega - \int_\Omega \delta v_i \rho \dot{v}_i \, d\Omega = 0
\end{aligned} \tag{6}$$

The above is known as the *principle of virtual power*, and is in fact the weak form of the momentum equation with the traction boundary conditions. *Now we may consider the current domain as an assemblage of finite elements.* We consider the coordinates of nodes by x_i^I, where

the superscript ranges from 1 to n_N (number of nodes). We will then use the shape functions $N^I(\mathbf{X})$ to interpolate the displacement and the virtual velocities between the nodal values as:

$$\begin{aligned} u_i(\mathbf{X},t) &= \sum_{I=1}^{n_N} N^I(\mathbf{X}) u_i^I(t) \\ \delta v_i(\mathbf{X},t) &= \sum_{I=1}^{n_N} N^I(\mathbf{X}) \delta v_i^I(t) \end{aligned} \tag{7}$$

Accordingly, the discrete form of the principle of virtual power can be written as:

$$\begin{aligned} &\sum_e \int_{\Omega_e} \sigma_{ij}\left(\boldsymbol{\varepsilon}(\mathbf{u})\right) N^I_{,j} \delta v_i^I \, d\Omega + \sum_e \int_{\Omega_e} \rho N^J N^I \ddot{u}_i^J \delta v_i^I d\Omega \\ &-\sum_e \int_{\Omega_e} \rho b_i N^I \delta v_i^I d\Omega - \sum_e \int_{\Gamma^*_{t_e}} \overline{t}_i^* N^I \delta v_i^I d\Gamma = 0 \end{aligned} \tag{8}$$

The subscript '*e*' denotes an individual element. Since the virtual displacements (test functions) are arbitrary for all nodes (except for the boundary) we may write:

$$\begin{aligned} &\sum_e \int_{\Omega_e} \sigma_{ij}\left(\boldsymbol{\varepsilon}(\mathbf{u})\right) N^I_{,j} d\Omega + \sum_e \int_{\Omega_e} \rho N^J N^I \ddot{u}_i^J d\Omega \\ &-\sum_e \int_{\Omega_e} \rho b_i N^I d\Omega - \sum_e \int_{\Gamma^*_{t_e}} \overline{t}_i^* N^I d\Gamma = 0 \qquad \forall (I,i) \notin \Gamma_{v_i} \end{aligned} \tag{9}$$

Since the stress tensor is a function of the strain tensor (which in turn is a function of displacements) the above is a system of nonlinear equations which can be solved using the Newton-Raphson method (Belytschko et al., 2000 ; Gullerud et al., 2004).

$$\begin{aligned} &\sum_e \int_{\Omega_e} \sigma_{ij}\left(\boldsymbol{\varepsilon}\left(u_i^I + du_i^I\right)\right) N^I_{,j} d\Omega - \sum_e \int_{\Omega_e} \rho N^I b_i d\Omega \\ &+\sum_e \int_{\Omega_e} \rho N^J N^I \ddot{u}_i^J d\Omega - \sum_e \int_{\Gamma^*_{t_e}} \overline{t}_i^* N^I d\Gamma = 0 \\ &\sum_e \int_{\Omega_e} \left\{ \sigma_{ij}\left(\boldsymbol{\varepsilon}\left(u_i^J\right)\right) + \frac{\partial \sigma_{ij}}{\partial \varepsilon_{kl}} \frac{\partial \varepsilon_{kl}}{\partial u_m^J} du_m^J \right\} N^I_{,j} d\Omega \\ &+\sum_e \int_{\Omega_e} \rho N^J N^I \ddot{u}_i^J d\Omega - \sum_e \int_{\Omega_e} \rho N^I b_i d\Omega - \sum_e \int_{\Gamma^*_{t_e}} \overline{t}_i^* N^I d\Gamma = 0 \end{aligned} \tag{10}$$

In order to carry out the differentiation of the strain tensor we use the kinematic equations to give,

$$\begin{aligned}
&\varepsilon_{kl} = \frac{1}{2}(u_{k,l} + u_{l,k}), \quad u_i(\mathbf{x}) = \sum_{I=1}^{n} N^I(\mathbf{x}) u_i^I \\
&\Rightarrow \varepsilon_{kl} = \frac{1}{2}\sum_{I=1}^{n}\left(\frac{\partial N^I}{\partial x_l}u_k^I + \frac{\partial N^I}{\partial x_k}u_l^I\right) \\
&\frac{\partial \varepsilon_{kl}}{\partial u_m^J} = \frac{1}{2}\sum_{I=1}^{n}\left(\frac{\partial N^I}{\partial x_l}\delta_{IJ}\delta_{km} + \frac{\partial N^I}{\partial x_k}\delta_{IJ}\delta_{lm}\right) \equiv \frac{1}{2}\sum_{I=1}^{n}\left(\frac{\partial N^J}{\partial x_l}\delta_{km} + \frac{\partial N^J}{\partial x_k}\delta_{lm}\right)
\end{aligned} \tag{11}$$

Hence, we may rewrite Eq. (10) as follows,

$$\begin{aligned}
&\sum_e \int_{\Omega_e}\left\{\sigma_{ij}\left(\boldsymbol{\varepsilon}\left(u_i^J\right)\right) + \frac{\partial \sigma_{ij}}{\partial \varepsilon_{ml}}\left[\frac{1}{2}\left(\frac{\partial N^J}{\partial x_l}\right)\right]du_m^J + \frac{\partial \sigma_{ij}}{\partial \varepsilon_{km}}\left[\frac{1}{2}\left(\frac{\partial N^J}{\partial x_k}\right)\right]du_m^J\right\}N_{,j}^I d\Omega \\
&+\sum_e \int_{\Omega_e} \rho N^J N^I \ddot{u}_i^J d\Omega - \sum_e \int_{\Omega_e} \rho N^I b_i d\Omega - \sum_e \int_{\Gamma_{t_e}^*} \overline{t}_i^* N^I d\Gamma = 0
\end{aligned} \tag{12}$$

in which we used the properties of the Kroneker Delta to change the indices of *epsilon* and *N*. Now we change the dummy index *k* to *l* and rearrange the terms as follows:

$$\begin{aligned}
&\sum_e \int_{\Omega_e}\left\{\sigma_{ij}\left(\boldsymbol{\varepsilon}\left(u_i^J\right)\right) + \frac{\partial \sigma_{ij}}{\partial \varepsilon_{ml}}\frac{\partial N^J}{\partial x_l}du_m^J\right\}N_{,j}^I d\Omega \\
&+\sum_e \int_{\Omega_e} \rho N^J N^I \ddot{u}_i^J d\Omega - \sum_e \int_{\Omega_e} \rho N^I b_i d\Omega - \sum_e \int_{\Gamma_{t_e}^*} \overline{t}_i^* N^I d\Gamma = 0
\end{aligned} \tag{13}$$

Another changing of the dummy index *m* to *k* for convenience, results in,

$$\begin{aligned}
&\sum_e \int_{\Omega_e}\left\{\sigma_{ij}\left(\boldsymbol{\varepsilon}\left(u_i^J\right)\right) + \frac{\partial \sigma_{ij}}{\partial \varepsilon_{kl}}N_{,l}^J du_k^J\right\}N_{,j}^I d\Omega \\
&+\sum_e \int_{\Omega_e} \rho N^J N^I \ddot{u}_i^J d\Omega - \sum_e \int_{\Omega_e} \rho N^I b_i d\Omega - \sum_e \int_{\Gamma_{t_e}^*} \overline{t}_i^* N^I d\Gamma = 0
\end{aligned} \tag{14}$$

With the definition of the *tangent stiffness matrix* and internal and external nodal forces, we may write the above as:

$$\begin{aligned}
&M^{JI}\ddot{u}_i^J + K_{ik}^{IJ}du_k^J + {}^{\text{int}}F_i^I - {}^{ext}F_i^I = 0 \qquad \forall(I,i) \notin \Gamma_{u_i} \\
&\mathbf{Ma} + \mathbf{K}d\mathbf{u} + \mathbf{f}^{\text{int}} - \mathbf{f}^{\text{ext}} = 0
\end{aligned} \tag{15}$$

For which we have,

$$
\begin{aligned}
M^{JI} &= \sum_e \int_{\Omega_e} \rho N^J N^I d\Omega \\
K_{ik}^{IJ} &= \sum_e \int_{\Omega_e} \frac{\partial \sigma_{ij}}{\partial \varepsilon_{kl}} N_{,j}^I N_{,l}^J d\Omega \\
{}^{\text{int}}F_i^I &= \sum_e \int_{\Omega_e} \sigma_{ij}\left(\boldsymbol{\varepsilon}\left(u_i^J\right)\right) N_{,j}^I d\Omega \\
{}^{ext}F_i^I &= \sum_e \int_{\Omega_e} \rho b_i N^I d\Omega + \sum_e \int_{\Gamma_{t_e}^*} \overline{t}_i^* N^I d\Gamma
\end{aligned}
\tag{16}
$$

A key element in the above expressions is the derivative of the stress tensor with respect to the strain tensor. If plastic deformation is considered as the source of nonlinearity, the stress tensor would become a function of the *strain-tensor increment* (which in turn is a function of the *displacement increment*), defined over a time increment Δt , for which we have:

$$
\begin{aligned}
K_{ik}^{IJ} &= \int_\Omega C_{ijkl} N_{,j}^I N_{,l}^J d\Omega \equiv \int_\Omega \frac{\partial \sigma_{ij}}{\partial \Delta \varepsilon_{kl}} N_{,j}^I N_{,l}^J d\Omega \\
{}^{\text{int}}F_i^I &= \int_\Omega \sigma_{ij}\left(\Delta\boldsymbol{\varepsilon}\left(\Delta u_i^J\right)\right) N_{,j}^I d\Omega \\
{}^{ext}F_i^I &= \int_\Omega \rho b_i N^I d\Omega + \int_{\Gamma_i^*} \overline{t}_i^* N^I d\Gamma
\end{aligned}
\tag{17}
$$

Here a main difficulty is to compute the stress caused by the incremental strain through the integration of the plastic stress-strain equations. On the other hand, the dynamic nature of the problem requires progression of the solution in time domain, for which we have explicit and implicit time integration methods. The explicit algorithms remove the need to invert the stiffness matrix in every time step by de-coupling the equilibrium equations. However, they are *conditionally* stable and the length of the time step must be smaller than a critical value to ensure that the solution converges. Hence, explicit algorithms are generally used for problems which by nature require small time steps, such as wave propagations, shock responses, and explosive or impact loadings.

The implicit algorithms are unconditionally stable and the maximum time step is governed by accuracy considerations. However, they require inversion of the stiffness matrix at every time step and this significantly increases the cost of computations. However, the time step length can be substantially larger thereby reducing the overall number of time steps. Thus, implicit algorithms are suitable for dynamic problems where the responses involve low frequency components, such as seismic responses or large deformations of elasto-plastic components under ramp or step loadings (Gullerud et al., 2004).

3.3 A Treatise of Related Fracture Parameters

Fracture is the separation of a component into, at least, two parts. This separation can also occur locally due to formation and growth of cracks. The crack propagation can occur in many ways, for instance we may have fast-unstable and slow-stable crack growth under monotonic loading or a cyclic growth under alternating loads. Based on Fracture Mechanics principles an energy criterion for the onset of crack growth can be defined in the following general form:

$$G = -\frac{d\Pi}{dA} \geq R \tag{18}$$

in which G is called the *energy release rate* (also known as the *crack driving force*), A is the cracked area, and R is the resistance of the material to crack growth. The energy release rate, G, can be considered as the energy *source* for the crack growth and may be obtained from the stress analysis of the cracked geometry. On the other hand, the resistance to crack growth (R) can be considered as the energy *sink* and depends on the operating ***fracture mechanism***. It should be mentioned that the latter depends on many factors including: the chemical composition and microstructure of the material, temperature, environment, loading rate, and the state of stress. The resistance to crack growth can be defined by a special term called the *toughness* of the material. We should also distinguish between *ductile* and *brittle* as two different types of fracture. By definition, ductile fracture is always accompanied by a *significant* amount of plastic deformation, while brittle fracture is characterized by very little plastic deformation. It should be noted that due to finite strength of materials, there is always a small *damaged* zone around the crack tip. For metals, this damaged zone is referred to as the *crack tip plastic zone*. If the size of the plastic zone is small we may use Linear Elastic Fracture Mechanics (LEFM) parameters like G and K (energy release rate and stress intensity factor respectively). Nevertheless, for large plastic zone conditions the linear elastic assumptions are not correct, i.e., LEFM is not applicable and nonlinear models must be used. If this nonlinearity is not very significant, it can be handled with a *non-linear elastic* model, for which a non-linear-elastic energy release rate called J (usually known as the J-Integral) is used. However, we should note that similar to the LEFM, there is a limit to the validity of J with regard to the size of the plastic zone. Thus for situations where the crack tip plasticity is wide-spread the appropriate parameter is the crack-tip opening displacement or angle (CTOD and CTOA respectively).

3.3.1 CTOA Methodology for FE Simulations of Ductile Crack Growth

Both CTOD and CTOA can be used for determination of the onset of crack growth in ductile fracture problems. However, for problems that involve both initiation and growth phases, it has been shown that modeling approaches based on CTOA can provide a viable growth criterion for thin materials (Gullerud et al., 1999). Using the FE method, the CTOA is defined by nodal displacements normal to the crack plane (Gullerud et al., 1999, 2004). For 2D planar problems the CTOA can simply be considered as the angle defined by the first nodal displacement, one element back from the crack tip. Note that the CTOA (as defined for WARP3D FE code and used here) is the full angle from one crack face to the other. The CTOA-controlled crack growth operates by advancing the crack front a prescribed distance when the CTOA reaches a specified *critical* value.

The critical CTOA is calculated from the critical CTOD, which is a measure of fracture toughness. Fracture toughness for a specific material can vary with the thickness, strain rate, temperature, etc. The general methodology for using a calibrated value of critical CTOA for an arbitrary component made of a specific material can be summarized as: (a) obtain well characterized experimental fracture test data with crack tearing up to and beyond maximum load; (b) analyze the tests with elastic–plastic CTOA controlled crack-tearing finite element analysis with crack front modeling, mesh size, and material model of sufficient fidelity to

represent the tests; (c) iterate the FEA with an assumed CTOA value until the results are close to the experimental data in predicting deformation, strains, maximum load and also are reasonably close in predicting the trends and amount of crack growth; (d) use this calibrated CTOA value, material data, and mesh size to predict crack tearing fracture behavior for other types of specimens or applications (Gullerud et al., 1999).

3.3.2 Crack Growth Simulation using Cohesive Elements

In simulations of ductile crack growth there are instances that a single-parameter treatment of cracked bodies may not yield accurate results in presence of widespread yielding. The remedy is to use either two-parameter fracture mechanics methods (like the J-Q approach) or other solutions based on damage mechanics models (Anderson, 1994; Cornec et al., 2003). Among the latter, the cohesive model with interface elements seems very attractive because it is computationally efficient and its two parameters can be determined with relative ease. In this approach, the crack extension evolves as a direct outcome of the computations by creation of new traction free crack faces. This method has been formulated in WARP3D to provide it with the capability to simulate mixed mode crack growth, and also phenomena such as crack turning and branching (Gullerud et al., 2004). In general, the interface elements consist of two surfaces which connect the faces of two adjacent solid elements. The crack propagation occurs when the energy release rate reaches a critical value (G_c). The implementation of interface elements requires a *cohesive constitutive relation* which in WARP3D is defined as a traction-separation relationship of the form:

$$t = \exp(1.0)\sigma_c \frac{\delta}{\delta_c} \exp\left(-\frac{\delta}{\delta_c}\right) \tag{19}$$

In the above, t is the effective traction between the two surfaces of an interface element, σ_c is the peak traction which shows the local material strength, δ is the effective opening displacement, and δ_c denotes the value of δ at the point of peak traction. The *cohesive fracture energy* can be described by:

$$\Gamma_c = \exp(1.0)\sigma_c \delta_c \tag{20}$$

Using the procedure outlined by Li and Siegmund (2002) for thin-sheet ductile material in plane stress condition, the cohesive strength can be selected as $\sigma_c = 2\sigma_y$, where σ_y is the yield stress of the bulk material. Another key parameter is the length of the cohesive zone which is defined as the distance from the crack tip to the point where the maximum cohesive traction is attained. In order to obtain accurate results using the cohesive zone model (CZM), the tractions in the cohesive zone must be represented properly by the FE spatial discretization, i.e., a minimum number of elements is required to resolve the variations within the cohesive zone (Falk et al., 2001).

4. Practical Examples of FE Simulation

The following sections present two practical examples of FE simulations of deformation and fracture of thin tubes under internal gaseous detonation. The simulations are carried out for an experimental detonation tube and an exploded gas cylinder.

4.1 Elastodynamic Response of an Aluminum Tube (Mirzaei & Karimi, 2006b)

This section presents the FE analysis of the elastodynamic response of an aluminum tube *without* flaw using WARP3D (a 3D research code for dynamic nonlinear fracture analysis of solids). In this code the nonlinear dynamic equilibrium equations are solved using an incremental-iterative *implicit* formulation with full Newton iterations to eliminate residual nodal forces (Gullerud et al., 2004). Although for this case study axisymmetric elements and *explicit* time integration scheme are the most appropriate choices, the aim of this initial analysis was to obtain a *validated 3D model* before attempting the crack growth simulation. The model consisted of 29400 8-node brick elements. The element distribution in the radial, longitudinal, and circumferential directions was 5, 280, and 21 respectively. A major part of the FE simulation was the modeling and preconditioning of a moving pressure load with the required profile. The detonation loading history was preconditioned as a discrete version of the exponential approximation to the Taylor-Zeldovich model and was prescribed as a function of time at each node. The results of the FE simulation included the initial detonation loading and the subsequent *reflections of the flexural waves* at the flanges. In Fig.5 the FE results are compared with the experimental results of Chao (2004). It is clear that there is a very good agreement between the results over this time interval.

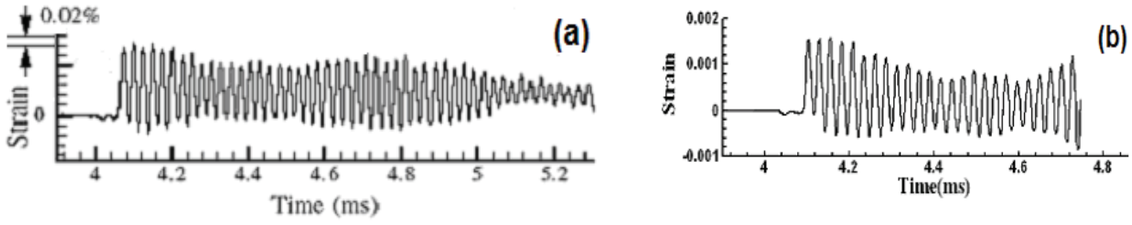

Fig. 5. (a): Experimental result (Chao, 2004) (b): WARP3D solution (Mirzaei & Karimi, 2006b).

4.2 Crack Growth Simulation for an Aluminum Tube (Mirzaei & Karimi, 2006b)

In the FE model of the pre-cracked tube the size of the far-field mesh was set to allow the simulation of the flexural (breathing mode) waves (in the form of hoop strains) so that they can be compared with the experimental strain signals. An upper bound of the mesh size was estimated using flexural wavelength. Because of the restrictions imposed by the CTOA approach, the crack front could not contain convenient collapsed elements that are used in computational fracture mechanics. Thus, the size of the elements near the crack tip was set small enough to capture the crack front plasticity and to maintain the accuracy of CTOA approach. In his experimental study, Chao (2004) used an axially oriented external notch, shaped as a semi elliptical surface crack. However, the finite element modeling of a semi elliptical surface crack, 35.2 mm long and 0.64 mm deep within a 0.89 mm wall thickness, could cause severe problems with regards to the shape and aspect ratios of the elements.

Therefore, the initial flaw was modeled by considering an equivalent through thickness crack. In practice the remote loading process was controlled so that the loading increments acting at the crack tip were not so large to cause large deformations in the crack tip elements in one loading step. This phenomenon is referred to as *overshoot* (Gullerud et al., 2004). Options are provided in the WARP3D code to control overshoot by restricting the size of one loading step based on projecting the expected CTOA from the previous load step. A control for general reduction of the step loading schedule is also available. But these approaches were not applicable in this study because they interfere with the simulation of detonation as a moving pressure load. In general, the "overshoot control" and the "automatic load reduction" change the load step, thereby affecting the detonation simulation. Thus, the load step size was substantially decreased to avoid the overshoot, resulting in prolonged runtimes.

4.2.1 Estimation of critical CTOA

Unfortunately, a CTOA calibration for the material in question is not available for such *high strain rates*. Hence, the critical CTOA was inferred from the experimental results as follows. Table 1 shows the experimental conditions and results for the pre-flawed aluminum tubes.

Shot	***d***	***2a***	***h***	V_{cj}	P_{cj}	***L***	***Fracture behavior***
	mm	*mm*	*mm*	*m/s*	*MPa*	*mm*	
30	0.64	35.2	0.89	2384	4.0	610	Crack confined in notch
34	0.64	35.2	0.89	2404	6.1	610	Forward and Backward growth

Table 1. Experimental conditions and fracture behavior for a pre-flawed aluminum tube (Chao, 2004).

The results indicate that in shot 30 the crack slightly advanced but remained confined within the notch, which indicates initiation plus a little propagation. Thus, shot 30 was recognized suitable for predicting the critical CTOA under actual dynamic condition that satisfies all of the loading rate and component thickness expectations for fracture toughness. The experimental results indicated that the crack remained confined in the notch exactly 0.2 ms after arrival of detonation loading. Thus, an initial FE simulation was carried out for this time period and the resulting maximum value of CTOA (4.61 degrees) was used as "dynamic critical CTOA" in the crack growth simulation for Shot 34 (see Table 1). Fig. 6 shows the results obtained from transient modeling of the moving pressure with full-dynamic effects.

As depicted in Fig. 6, the detonation front travels from left to right and causes a pattern of flexural structural waves as it proceeds toward the left crack tip. Also, it is clear the crack grows more in the forward direction, i.e., in the direction of movement of the detonation front. The same phenomenon was observed by Chao and shepherd in their experiments (Chao & Shepherd, 2005).

This asymmetric growth, which is one of the specific features of detonation-driven fracture of tubes and occurs quite naturally as a result of the difference between the relative speeds of the structural waves with respect to the two crack tips, will be discussed in sequel.

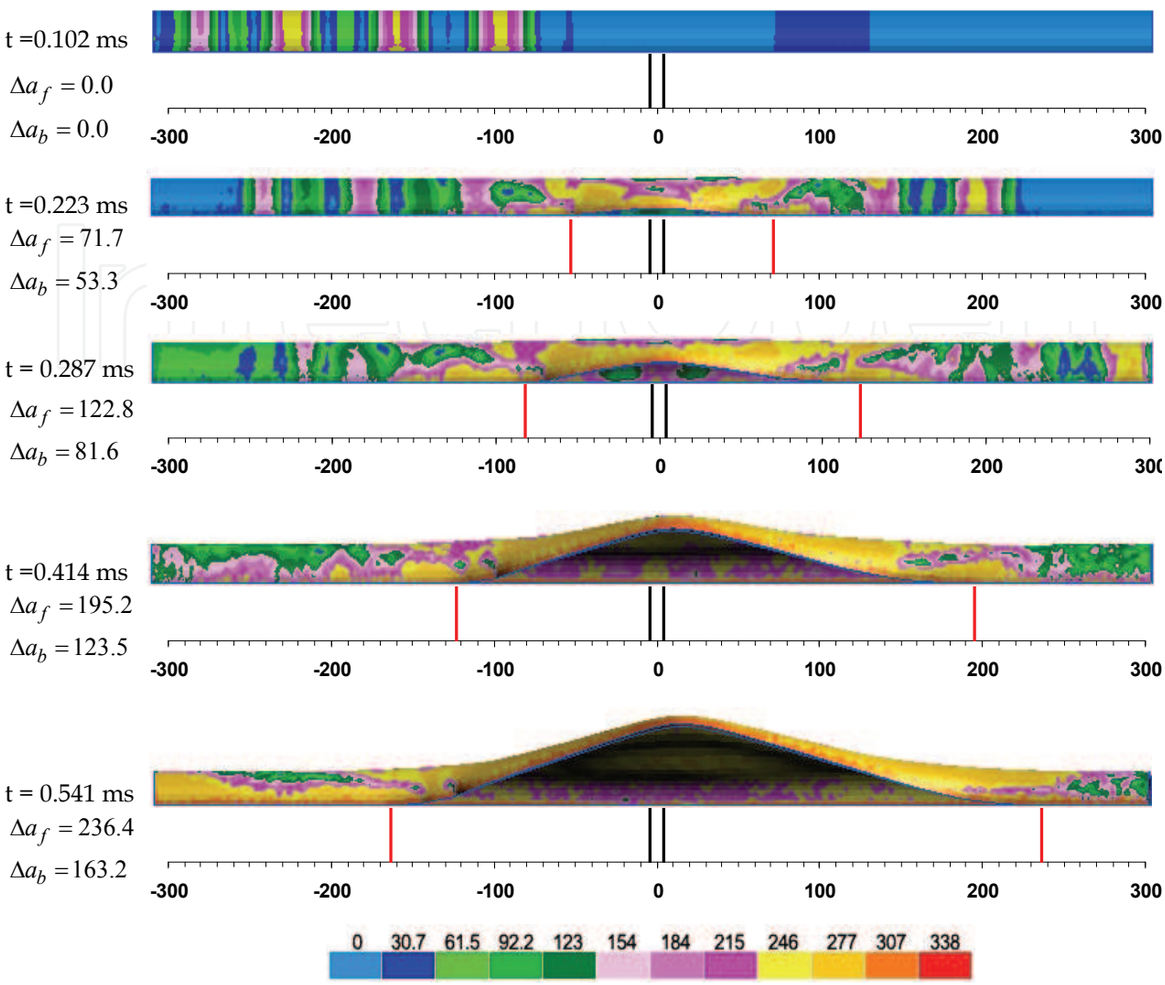

Fig. 6. Snapshots of simulated crack growth for an aluminum tube at different time intervals including the contours of the first principal stress component.

The simulations presented in Fig. 6 seem to be representative of a number of actual growth characteristics including flap bulging. Nevertheless, there are two major inconsistencies between the simulation results and the actual crack growth features. The first one is that the simulated crack speed is 2 times the actual average speed during the self-similar growth. The reason is that the retardation effects of cyclic crack growth were not considered in this analysis (Mirzaei et al., 2009). The second problem is that crack curving and branching could not be simulated using the CTOA approach implemented in WARP3D.

4.3 Crack Growth Simulation for an Aluminum Tube (Cirak et al., 2007)

Cirak et al. (2007) performed large-scale fluid-structure interaction simulation of viscoplastic deformation and fracturing of the experimental aluminum tube of Chao & Shepherd (2005). In practice, they used the static plain strain fracture toughness K_{Ic} to obtain the properties of their cohesive elements.

In general, their results showed some inconsistencies with the experiments, particularly with respect to the crack growth magnitude, speed, and premature cracking of the flap edges (see Fig.7). They also reported that their computational crack speeds were 2-3 times higher than experimentally observed (Deiterding et al., 2006).

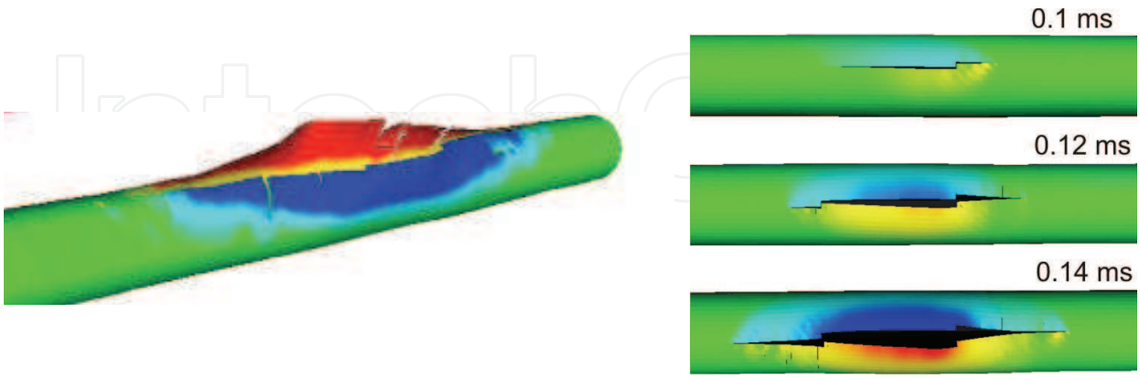

Fig.7. Crack growth simulation for an aluminum tube under internal gaseous detonation. Left: (Cirak et al., 2007). Right: (Deiterding et al., 2006)

4.4 FE Analysis of an Exploded Gas Cylinder (Mirzaei et al., 2009)

This section presents the finite element simulations of deformation and fracture of a gas cylinder which catastrophically failed as a result of an accidental explosion (see Fig.8). The results of a previous detailed investigation of this incident indicated that detonation of a low-pressure oxygen-rich mixture of hydrogen and oxygen was the cause of the cylinder failure (Mirzaei, 2008). The overall transient dynamic response of the cylinder to gaseous detonation loading was studied using the ANSYS/LS-DYNA V10 package and the crack growth simulations were performed using the WARP3D-R15 research code. The crack growth analyses were performed using interface cohesive elements. The accuracy of the finite element results was verified using analytical solutions and data collected from the remains of the cylinder.

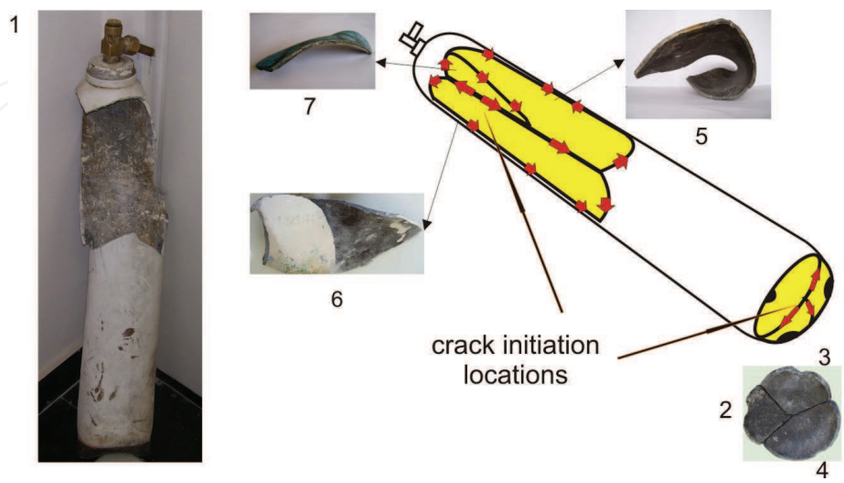

Fig. 8. Remains of an exploded gas cylinder along with a schematic showing the original locations of the collected fragments and the crack growth directions. The sketch is not to scale.

4.4.1 Elasto-plastic Dynamic Response

A transient elasto-plastic dynamic analysis was carried out to obtain the structural response of the cylinder to a moving pressure load with specific profile using 2011 rotary symmetric solid elements. The preconditioning and application of the loading history was similar to the procedure described for the aluminum tube before. The simulation was carried out for the detonation speed of 2300 m/s, initial pressure of 1.9 MPa, maximum pressure of 37 MPa, and exponential decay factor of T = 0.15 ms (Mirzaei, 2008). In order to validate the FE model, the results were compared with the analytical solutions reported in Refs (Mirzaei et al 2005; Mirzaei 2008b). To avoid the effects of the boundary conditions on the main signal, the results were compared at a distance of 200 mm from the upper neck. Fig.9 shows the results for a time period of 1ms, which includes the initial detonation loading and the subsequent reflections of the flexural waves.

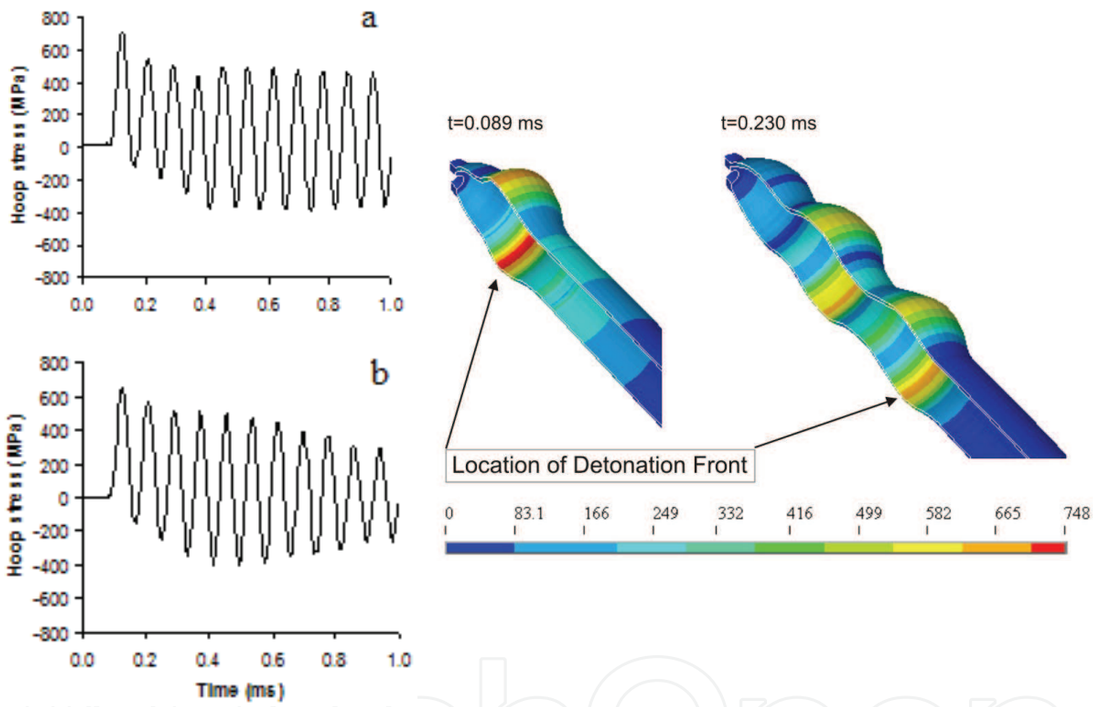

Fig. 9. Left: hoop stress vs. time at a distance of 200 mm from the upper neck. The results include the main signal (up to 0.35 ms) plus the reflected waves, a): elasto-dynamic solution (analytical), b): elasto-plastic dynamic solution (FE). Right: two snapshots showing the development of flexural waves with time and the related distributions of the Von-Mises stress (elasto-plastic dynamic FE). The stresses are in MPa.

The very good agreement between the two results for the main signal (the first 4 stress waves) is quite clear. However, the FE solution shows a stronger decay in the amplitude of the reflected waves. This can be attributed to the restraining effects of the bottom cap which was modeled as a simple support in the analytical solution. Fig. 9 also shows two snapshots of the development of flexural waves with time and the related distributions of the Von-Mises stress (elasto-plastic dynamic FE). It is clear that the maximum stress occurs at a

distance of 100 mm from the upper neck. This is the same location that the initiation of a 6-mm axial crack was recognized on the fragments Nos. 5 and 7 (see Fig.8).

4.4.2 Crack Growth Simulation

The dynamic mechanical properties of the cylinder material are shown in Table 2. The details of the experimental procedures were reported in (Mirzaei, 2008).

ρ	E	ν	σ_y	σ_u	K_c (h= 6 mm)
kg/m^3	GPa		MPa	MPa	$MPa\sqrt{m}$
8000	206	0.33	598	700	72

Table 2. Mechanical properties for the cylinder material (carbon steel).

Accordingly, the cohesive energy for crack growth was computed as

$$\Gamma_c = G_c = \frac{K_c^2}{E} = 25.16 \text{ kJ/m}^2 \tag{21}$$

Although different models have been proposed to estimate the length of the cohesive zone, the two most commonly used models in the literature are proposed by Hillerborg et al. (1976) and Rice (1979). The simulations reported here are based on the Hillerborg's model in which the cohesive zone length is expressed by:

$$l_{cz} = E\frac{G_c}{\sigma_c^2} \tag{22}$$

In this study 7-8 elements were used over the cohesive zone length to be able to fully resolve the variations within this zone. Fig.10 depicts the snapshots of simulated crack growth at different time intervals showing the contours of the first principal stress component. *The successive opening and closing of the crack flaps is a clear indication of a cyclic crack growth governed by the flexural waves*. Also, it is clear the crack grows more in the forward direction, i.e., in the direction of movement of the detonation front. The same phenomenon was observed by Chao and shepherd in their experiments (Chao, 2004; Chao & Shepherd 2005). This asymmetric growth occurs quite naturally as a result of the difference between the relative speeds of the structural waves with respect to the two crack tips. Let us denote the speed of the structural waves, the forward tip, and the backward tip by V_{sw}, V_{ft}, and V_{bt} respectively. In practice, the speed at which each stress cycle outdistances from the forward tip is; $V_{sw} - V_{ft}$, which is naturally less than $V_{sw} + V_{bt}$ (the speed of separation between the flexural wave and the backward tip). Hence, the *effective* time that each stress cycle acts on crack tips is longer for the forward tip.

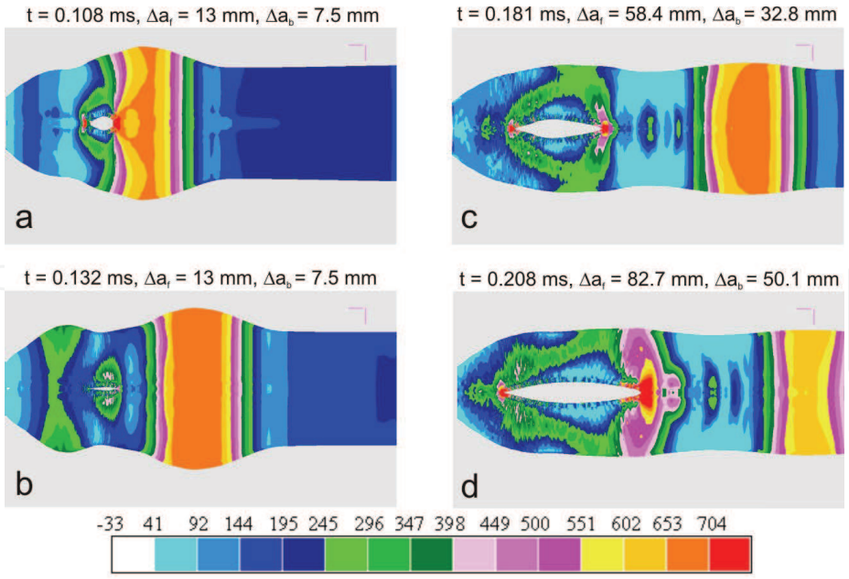

Fig. 10. Snapshots of simulated crack growth at different time intervals showing the contours of the first principal stress component. The movement of the detonation front is from left to right. The stresses are in MPa.

Although the simulations presented in Fig. 10 seem to be representative of a number of actual growth characteristics, there are major inconsistencies between the simulation results and the actual crack growth features. The most important one is that the simulated crack speed is 3 times the actual average speed during the self-similar growth. Another problem is that the crack branching does not occur at the actual location. These inconsistencies show that the implemented approach has not been able to model all the features of the cyclic crack growth mechanism. The remedy is that the growth retardations imposed by various *fatigue crack closure* mechanisms should be incorporated in the FE simulations.

4.4.3 Crack Growth Simulation with Retardation

In practice, the high amplitude stress cycles (caused by high-speed pressure) create an extreme low cycle fatigue (LCF) crack growth problem which can be represented by the upper portions of the Region III on the classical fatigue crack growth rate diagrams. In this Region the static modes of crack propagation are also operative, and because of high amounts of plastic deformation at the crack tip and the resultant plastic stretches on the crack wake the main retardation mechanism is the *plasticity-induced crack closure* (Anderson, 1995). Under these conditions, a cycle by cycle FE simulation of crack closure is the best practice. However, such simulation requires specific FE formulation for the cohesive elements. Thus, as an initial step, the closure effects were artificially incorporated into the WARP3D model by increasing the critical energy release rate in every increment. Accordingly, the cohesive parameters of the elements in front of the crack tip were proportionally increased to maintain the same stiffness in the linear part of traction-separation model after every incremental growth. Fig. 11 shows 4 snapshots of simulated crack growth with retardation at different time intervals including the contours of the first principal stress.

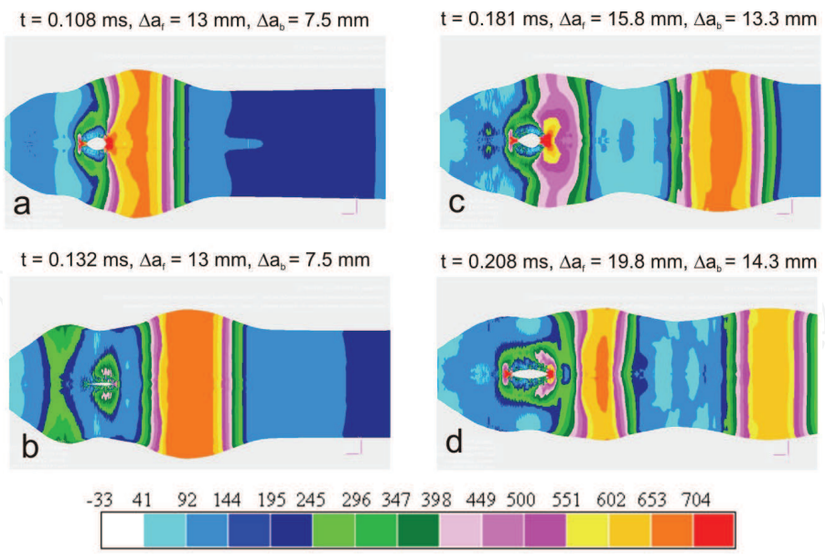

Fig. 11. Snapshots of simulated crack growth with retardation at different time intervals showing the contours of the first principal stress. The movement of the detonation front is from left to right. The stresses are in MPa.

In practice, the incorporation of retardation effects not only adjusted the overall crack speed but also resulted in crack curving and branching at the expected location. It is interesting to note that because of the growth retardation caused by closure mechanisms the crack experiences a relatively larger number of cycles to grow to a certain length. Accordingly, the cyclic bulging of the crack flaps can expand to the extent that the resultant axial stresses are significant enough to cause curving and branching. Fig. 12 also shows the onset of a second branching similar to the one that actually occurred in the exploded cylinder (see Fig.8).

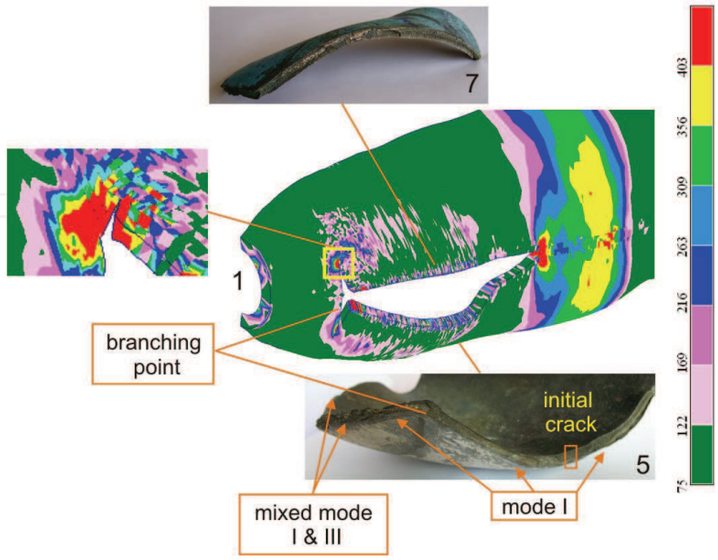

Fig. 12. Simulation of crack flap bulging and the resultant crack branching. The onset of the second branching is also visible in the magnified image of the upper branch. The stresses are in MPa.

5. Conclusions and Some Avenues for Future Research

The structural response of a cylindrical tube to internal moving pressure depends on several parameters including the dimensions and mechanical properties of the tube as well as the magnitude and speed of the moving pressure. For instance, high-speed traveling of relatively *low pressures* (level 1) can result in a pattern of fluctuating high frequency *elastic* strains. For the FE analysis of this problem an elastodynamic formulation with axisymmetric 2D elements and explicit time integration is quite appropriate. An interesting research activity in this area will be the investigation of the effects of successive gaseous detonations on the vibrational behavior of Pulse Detonation Engines.
Traveling of higher pressures (level 2), that can cause stresses in the order of the ultimate tensile strength of the material, may initiate axial cracks which with further propagation can result in *limited* fragmentation of the tube wall. Usually the initial cracks are created by local excessive shear and the self-similar crack propagation is governed by the structural waves. The FE analysis of this problem requires nonlinear dynamic elasto-plastic FE formulation with 3D elements, along with cohesive elements for crack initiation and growth simulation. It should be noted that a successful FE simulation of such crack growth should capture a number of specific features of detonation-driven fracture of cylindrical tubes. These features are:

a) Cyclic crack propagation during the self-similar growth of the axial crack
b) Cyclic bulging of the crack flaps
c) Crack curving and branching adjacent to the bulged area

It should be emphasized that, since a major portion of detonation-driven fracture of cylindrical tubes can involve *cyclic* crack growth, successful simulation of the fragmentation and accurate assessments of quantities like crack speed require specific procedures that suit this particular type of growth. This involves the implementation of specialized techniques in the modeling process plus the inclusion of retardation phenomena like fatigue crack closure. Unfortunately, the current commercial FE codes do not have built-in capabilities for such simulations.
Finally, traveling of *very* high pressures (level 3), that can cause stresses much higher than the ultimate tensile strength of the material, can simultaneously initiate several cracks in the tube wall. The rapid growth and branching of these cracks result in severe dynamic fragmentation. For this class of problems usually Lagrangian FE codes with explicit time integration along with simple failure criteria (like the equivalent plastic strain) are used. However, a main difficulty is that the problem can involve hundreds of thousands of time steps and millions of elements. Moreover, numerical instabilities caused by separation of several fragment of elements must be taken into account. In practice, nonlinear-explicit 3D finite element codes like DYNA3D and LS-DYNA provide many capabilities for such simulations.

6. References

Anderson, T.L. (1995). *Fracture Mechanics: Fundamentals and Applications*. 2nd ed. CRC Press. ISBN 0-8493-4260-0.

Beltman, W., Burcsu, E., Shepherd, J., & Zuhal, L. (1999). The structural response of cylindrical shells to internal shock loading. *Journal of Pressure Vessel Technology*, 121, pp. 315–322.

Beltman, W., & Shepherd, J. (2002). Linear elastic response of tubes to internal detonation loading. *Journal of Sound and Vibration,* 252 (4), pp. 617–655.

Belytschko, T., Liu, W.K., & Moran B. (2000). *Nonlinear finite element for continua and structures*. Wiley.

Chao, T.W., & Shepherd, J. E. (2005). Fracture response of externally flawed aluminum cylindrical shells under internal gaseous detonation loading. *International Journal of Fracture* ;134(1):59–90.

Chao, T.W., (2004) *Gaseous detonation-driven fracture of tubes.* PhD thesis, California Institute of Technology, Pasadena, California.

Cirak, F., Deiterding, R., & Mauch, SP. (2007). Large-scale fluid-structure interaction simulation of viscoplastic and fracturing thin-shells subjected to shocks and detonations. *Computers & Structures*; 85(11-14):1049–65.

Cornec, A., Scheider, I., & Schwalbe, K.H. (2003). On the practical application of the cohesive model. *Engineering Fracture Mechanics*. 70:1963-1987.

Deiterding, R., Cirak, F., & Meiron, D. (2006). Computational results for the fracturing tube validation experiment. *ASCI/ASAP Research review Caltech* http://www.cacr.caltech.edu/asc/wiki/pub/FracturingTube/WebHome/DetFracSim.ppt

Falk, M.L., Needleman,A., & Rice, J.R. (2001). A critical evaluation of cohesive zone models of dynamic fracture. *J Phys IV* Proc 2001:543–50.

Goto, D.M., Becker, R., Orzechowski, T.J., Springer, H.K., Sunwoo, A.J., & Syn, C.K.R. (2008). Investigation of the fracture and fragmentation of explosively driven rings and cylinders. *International Journal of Impact Engineering,* Vol.35, Issue 12, 1547-1556.

Gullerud, A.S., Koppenhoefer, K.C., Roy, A., & Dodd, Jr R.H. (2004). WARP3D: 3-D dynamic nonlinear fracture analysis of solids using parallel computers and workstations. Structural Research Series (SRS) 607, UILU-ENG-95-2012, University of Illinois at Urbana-Champaign.

Gullerud, A.S., Dodds, Jr R.H., Hampton, R.W., & Dawicke, D.S. (1999). Three-dimensional modeling of ductile crack growth in thin sheet metals: computational aspects and validation. *Engineering Fracture Mechanics,* 63:347-74.

Hillerborg, A., Modeer, M., & Petersson, P.E. (1976). Analysis of crack formation and crack growth in concrete by means of fracture mechanics and finite elements. *Cement and Concrete Research,* 6, 1976 :773-82

Li, W. & Siegmund, T. (2002). An analysis of crack growth in thin-sheet metal via a cohesive zone model. *Engineering Fracture Mechanics,* 69:2073-93.

Mirzaei, M., Mazaheri, K., & Biglari, H. (2005). Analytical modeling of the elastic response of tubes to internal detonation loading. *International Journal of Pressure Vessels and Piping,* Vol.82, No. 12, 883-895.

Mirzaei, M., Biglari, H., & Salavatian, M. (2006a). Analytical and numerical modeling of the elastodynamic response of a cylindrical tube to internal gaseous detonation. *International Journal of Pressure Vessels and Piping,* Vol.83, No.7, 531-539.

Mirzaei, M., Karimi, R. (2006b). Crack growth analysis for a cylindrical shell under dynamic loading., *Proceedings of ASME PVP 2006 / 11th International Conference on Pressure Vessel Technology, ICPVT-11*, Vancouver, Canada.

Mirzaei, M., Salavatian, M., & Biglari, H. (2006c). Simulation of fatigue crack growth in a detonation tube. *Proceedings of ASME PVP 2006 / 11th International Conference on Pressure Vessel Technology, ICPVT-11*, Vancouver, Canada.

Mirzaei, M. (2008a). Failure analysis of an exploded gas cylinder. *Engineering Failure Analysis,* Vol.15, No.7, 820-34.

Mirzaei, M. (2008b). On amplification of stress waves in cylindrical tubes under internal dynamic pressures. *International Journal of Mechanical Sciences* Vol.50, No.8, 1292-1303.

Mirzaei, M., Harandi, A., & Karimi, R. (2009). Finite element analysis of deformation and fracture of an exploded gas cylinder. *Engineering Failure Analysis* Vol.16, 1607-1615.

Naitoh, M., Kasahara, F., Kubota, R., & Ohshima, I. (2003). Analysis of pipe rupture of steam condensation line at Hamoaka-1, (I) accumulation of non-condensable gas in a pipe. *Journal of Nuclear Science and Technology*,Vol.40, No.12, 1032.

Price, W.H. (2006). An acetylene cylinder explosion: A most probable cause analysis. *Engineering Failure Analysis,* Vol.13, No., 705-715.

Reismann, H. (1965). Response of a pre-stressed cylindrical shell to moving pressure load. *Proceedings of Eighth Midwest Mechanics Conference,* S. Ostrach and R. Scanlon, Eds., Pergamon Press, 1965, pp. 349–363.

Rice, JR. (1979). The mechanics of earthquake rupture. *Proceedings of the international school of physics ''Enrico Fermi''*, Course 78, 1979. Italian Physical Society/North-Holland; 1980: 555–649.

Soto, O., Baum, J., & Löhner, R. (2010). An efficient fluid–solid coupled finite element scheme for weapon fragmentation simulations. *Engineering Fracture Mechanics.* Vol.77, 549-564.

Tang, S. (1965). Dynamic response of a tube under moving pressure. *Proceedings of the American Society of Civil Engineers,* vol. 5, Engineering Mechanics Division, 1965, pp. 97–122.

Finite Element Analysis

Edited by David Moratal

ISBN 978-953-307-123-7

Hard cover, 688 pages

Publisher Sciyo

Published online 17, August, 2010

Published in print edition August, 2010

Finite element analysis is an engineering method for the numerical analysis of complex structures. This book provides a bird's eye view on this very broad matter through 27 original and innovative research studies exhibiting various investigation directions. Through its chapters the reader will have access to works related to Biomedical Engineering, Materials Engineering, Process Analysis and Civil Engineering. The text is addressed not only to researchers, but also to professional engineers, engineering lecturers and students seeking to gain a better understanding of where Finite Element Analysis stands today.

How to reference

In order to correctly reference this scholarly work, feel free to copy and paste the following:

Majid Mirzaei (2010). Finite Element Analysis of Deformation and Fracture of Cylindrical Tubes under Internal Moving Pressures, Finite Element Analysis, David Moratal (Ed.), ISBN: 978-953-307-123-7, InTech, Available from: http://www.intechopen.com/books/finite-element-analysis/finite-element-analysis-of-deformation-and-fracture-of-cylindrical-tubes-under-internal-moving-press

INTECH
open science | open minds

InTech Europe
University Campus STeP Ri
Slavka Krautzeka 83/A
51000 Rijeka, Croatia
Phone: +385 (51) 770 447
Fax: +385 (51) 686 166
www.intechopen.com

InTech China
Unit 405, Office Block, Hotel Equatorial Shanghai
No.65, Yan An Road (West), Shanghai, 200040, China
中国上海市延安西路65号上海国际贵都大饭店办公楼405单元
Phone: +86-21-62489820
Fax: +86-21-62489821

IntechOpen